3 Experiments in Subsonic Flows

The performance of the ALTP heat-flux gauge in subsonic, incompressible flow is demonstrated in the following sections. The first benchmark experiments are carried out in the flow of an internal ribbed channel representing the internal cooling passages of a gas turbine blade in a test rig of the Institute of Aerospace Thermodynamics (ITLR). Comparative measurements are made between the time-averaged values obtained using a single-point ALTP sensor and detailed global surface measurements using the transient thermal liquid crystal technique. In addition, time-resolved measurements are also corroborated with hot film measurements at the wall to better clarify the influence of unsteadiness in the velocity field at the wall on fluctuations in the heat flux.
The second benchmark investigates the external flow around a low aspect-ratio circular cylinder. The experiments shall demonstrate the use of the ALTP for distributed surface measurements by multiple single-point gages. The general purpose of this study is the detection of flow phenomena on the surface of a finite cylinder and the qualitative correlation of heat and pressure fluctuation quantities with oil-film visualization and static pressure measurements in order to to localize dominant flow features.

3.1 Heat Transfer Measurements on the Tip Wall of a Ribbed Channel

An increase of heat transfer levels in internal cooling passages of turbine blades leads to an higher overall efficiency of engines. To fully understand the heat loads in a system such as this, fluctuations in the heat flux can be equally or more important than the time-mean values. The identification of the range of frequencies present in the turbulence field and which of those frequencies are responsible for increasing heat transfer are of great interest. Many research groups have investigated heat transfer in internal passages; however, time-mean results for the tip wall of a two-pass high aspect ratio channel are very sparse. Time-resolved heat transfer turbulence spectra in gas turbine applications have been mainly investigated for external flows. In these studies, it was found that a strong

coherence between fluctuations at lower frequencies exists, indicating that the penetration of large-scale eddies through the boundary layer are responsible for augmentation of the heat transfer. A more detailed discussion including references on these subjects can be found in Roediger et al. [116] and Jenkins et al. [62]. The following experiments were carried out in close cooperation with S. Jenkins of ITLR.

3.1.1 Experimental Setup

Facility. Measurements are made on the tip wall of a 4:1 aspect ratio, two-pass channel. The channel, shown in Figure 3.1, is 2.4 m long and each pass has a width of W = 42 mm and height of H = 168 mm, resulting in a hydraulic diameter of D_h = 1.6 W = 67.2 mm. The inlet channel has an entrance length of 1.524 m to ensure hydrodynamically and thermally fully developed conditions preceding the measurement section with a length of 0.840 m. This length is required to accommodate 15 ribs. The inlet and outlet channels are connected by a sharp 180° bend. The divider wall has a thickness of $W_{web} = 0.4\,\mathrm{W}$ and the tip of the divider wall is radiused as shown in Figure 3.1. The ribs have a square cross section and a height of e/H = 0.05 (or e/D_h = 0.125) and a spacing of P/e = 10.

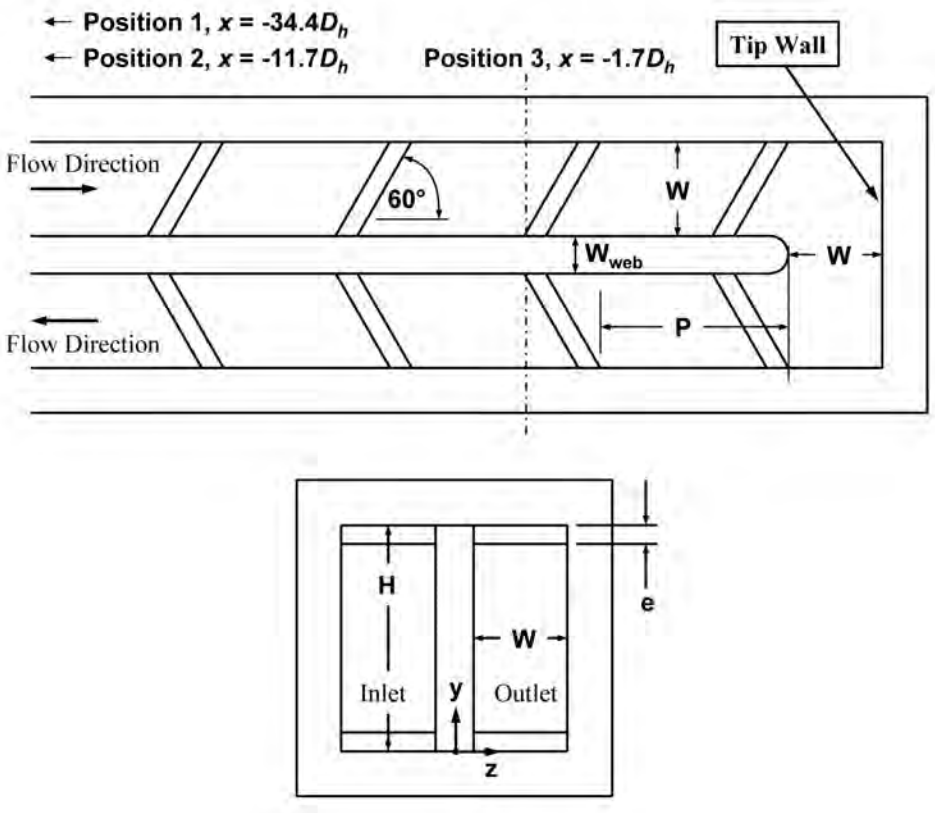

Figure 3.1: Schematic top view and cross section of the test channel with 60 deg ribs.

They are arranged in a parallel fashion at an angle of 60° to the flow direction.
The temperature step is provided by a mesh heater, which is square in cross section and the outlet of the channel is connected by a series of pipes to a vacuum pump system. The piping system includes a Venturi nozzle for measurements of the mass flow rate and also contains a valve for flow regulation.

Instrumentation. Narrow band liquid crystals (Hallcrest BM/R31C1W/C17-10) are used to determine the heat transfer coefficient distribution on the tip wall. A CCD camera (Sony RBG Video Camera Module, Model XC-711P) is positioned to capture the color change of the liquid crystal on the tip wall during the transient experiment. The channel is constructed from 20 mm thick Plexiglas to offer good optical access and to fulfill the required semi-infinite wall assumption and convective boundary condition assumed with this method. For more information on data analysis and reduction of TLC, the reader is referred to section A.1.3.
Measurements of the centerline temperature are made with thermocouples placed at $34.4\,D_h$, $11.7\,D_h$, and $1.7\,D_h$ upstream of the bend in the inlet channel. This temperature data is used to account for the variation in bulk temperature both with position and time T_B (x,t). Further information on the calculation of the bulk temperature history and bulk velocity can be found in [62] and references therein.
Uncertainties related to the TLC heat transfer measurements are based on temperature, time, and material property uncertainties. The resulting total uncertainty in the Nusselt number is about 8% according to Jenkins et al. [62].
In the present experiments, an ALTP sensor with a protective coating and an active area of 3×3 mm^2 is used. For comparison with the fluctuations measured by the ALTP, a hot film gauge (DANTEC Flush Mounting Probe 55R45) with an active length of 0.4 mm operated by a DANTEC 56C20 temperature plug-in unit in a DANTEC 56C01 CTA system is used to measure velocity fluctuations at the same location at the tip wall in successive runs. More information on the working principle of hot-film gauges can be found in Appendix A.1.

Computation of turbulence quantities. Fluctuations in the velocity and heat flux are calculated from the integration of the power spectral density as follows:

$$u'^2 = \int_0^\infty \xi_u(f)df \ , \ q'^2 = \int_0^\infty \xi_q(f)df, \tag{3.1}$$

With these quantities, the turbulence intensity and turbulent heat flux intensity are computed using the rms-values divided by the mean:

$$Tu = \frac{\sqrt{u'^2}}{u_m} \ , \ Tu_q = \frac{\sqrt{q'^2}}{q_m} \tag{3.2}$$

The integral time scale is computed from an integration of the autocorrelation function from the time signal of the velocity or heat flux where the autocorrelation function is computed from the normalized data,

$$R_{xx} = \int_0^\infty \hat{q}(t)\hat{q}(t+\tau)dt \ \text{ where } \ \hat{q}(t) = \frac{q(t) - q_m}{q'} \tag{3.3}$$

and where q_m is the mean of the heat-flux time signal and τ is the measurement interval. The autocorrelation function is integrated to determine the integral time scale as follows:

$$\Upsilon_q = \int_0^{\tau|R_{xx}=0} R_{xx}(\tau)d\tau \tag{3.4}$$

The same procedure is carried out for the velocity and the integral length scales Λ_f and Λ_q can be derived from this quantity by the use of an assumed representative bulk velocity (see Jenkins et al. [62]) as follows:

$$\Lambda_f = u_B\Upsilon_f, \ \Lambda_q = u_B\Upsilon_q, \tag{3.5}$$

The Kolmogorov scale is determined based on a point in the power density spectrum where the slope is approximately m = -5/3. This allows for the calculation of a turbulent dissipation, ε, and thereby a Kolmogorov length scale, i.e. in the equilibrium range acc. to Pope [109]:

$$\xi_u(k) = 0.5\varepsilon^{2/3}k^{-5/3} \tag{3.6}$$

and

$$\eta = \left(\frac{\nu^3}{\varepsilon}\right)^{1/4} \tag{3.7}$$

3.1.2 Experimental Results

Time-mean results The distribution of heat transfer coefficient Nu, shown in Figure 3.2, is representative of the typical pattern for the tip wall in this high aspect-ratio ribbed channel. The orientation of the figure is downstream towards the tip wall (see Fig. 3.1). Symmetric peaks in the heat transfer coefficient on the left side of the figure are due to the rib induced secondary flows. The ribs induce a flow along the ribbed walls from the divider wall to the outer wall which then recirculates back to the divider wall at the midplane, giving two symmetric secondary flow structures, shown in the schematic in the

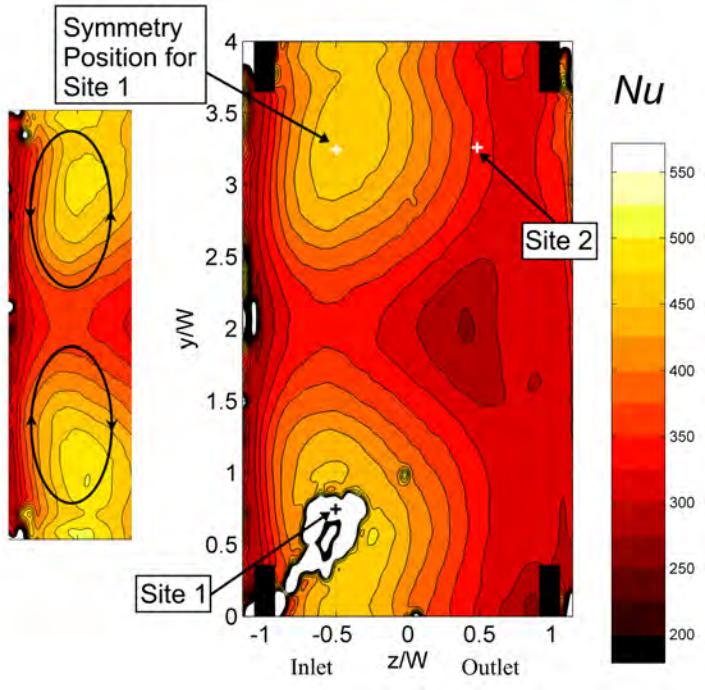

Figure 3.2: Distribution of Nusselt number on the tip wall at Re =100,000 and locations of Site 1 and 2 (black boxes in corners represent tip wall mounts which distort optical access); Distribution on left-hand side displays a schematic of secondary flow. [62]

figure. The impingement of the secondary flow vortices creates symmetric peaks of maximum heat transfer levels. In the bend region, these secondary flows are disrupted and on the outlet side of the tip wall, heat transfer levels are much lower.
The location of the ALTP sensor is shown with a black cross in the lower left corner, centered at roughly y/W = 0.7 and z/W = -0.5 and is referred to as Site 1. The sensor was placed in this position to take advantage of the symmetry of the results, thus allowing for a direct comparison between the ALTP and TLC results within the same experiment. This symmetry is shown in the schematic using results from a separate experiment without the heat-flux sensor installed. In this example, agreement between the two symmetric positions is within 1%. The sensor is also placed in this location with relatively high heat flux and low gradients to reduce uncertainties in the heat-flux measurements. Furthermore, the region of maximum heat transfer is fairly independent of the Reynolds number. The comparison of heat transfer coefficients measured by the TLC and the ALTP exhibits a very good agreement (see table 3.1). Hence, the procedure for determining the Nusselt number using the transient thermal liquid-crystal technique and the use of the ALTP heat-flux sensor at these heat transfer levels is validated. Furthermore, the repeatability of the measurements for two different sensors is verified (see table 3.1).

For a constant Reynolds number the heat transfer coefficient should remain constant for different temperature jumps. In table 3.2 the variation of the temperature from $\Delta T = (T_B - T_0) = 9.6\,K$ to $\Delta T = 22.5\,K$ demonstrates this characteristic for the ALTP. It should be noted that, due to the bulk fluid temperature rise during the test, the heat-flux sensor recorded a slowly increasing heat flux, however, the heat transfer coefficient or Nusselt number is found to be constant. A comparison for a range of Reynolds numbers

Sensor	Re [-]	$u_\infty \left[\frac{m}{s}\right]$	$h_{ALTP} \left[\frac{W}{m^2K}\right]$	$h_{TLC} \left[\frac{W}{m^2K}\right]$	difference [%]
788 II	100,000	22.7	194.6	193.6	0.5%
787 I	100,000	22.7	187.7	188.4	0.4%

Table 3.1: Repeatability of measurements and comparison of heat transfer coefficients for ALTP and TLC.

Sensor	$Re\,[-]$	$\Delta T\,[K]$	$h_{ALTP}\,[W/m^2K]$
788 II	200,000	9.6	297.6
788 II	200,000	22.5	295.4
		difference	= 1.0%

Table 3.2: Variation of temperature jump for $Re = 200,000$.

from Re=50,000 to 200,000 between the heat transfer coefficients from the ALTP and the symmetric point in the TLC distribution is shown in Figure 3.3(a). The data tracked very well over the entire range with a maximum difference of 6%. The mean heat transfer coefficient distributions obtained from TLC for the Reynolds numbers Re=50,000; 100,000; 150,000 and 200,000 can be found in Appendix A.4 and their detailed features are discussed by Jenkins et al. [62].

The heat flux is also measured for a second point positioned on the outflow side of the tip wall in the upper right corner Site 2, in Figure 3.2, where symmetry could also be used for comparisons. The time-mean results for this site are in good agreement as well. Figure 3.3(b) shows the Nusselt number for both measurement techniques at both Sites 1 and 2 in a log-log scale. The difference in slopes for the two sites can be seen in this figure. Different normalizations for channel flows can be found in literature. In Site 1, the flow experienced a condition similar to a jet stagnation point flow. A normalization proposed by Lee et al. [75] is found to be most appropriate [62]. The Nusselt number at the stagnation point of a jet (for high Reynolds numbers) varies according $\mathrm{Nu} \propto \mathrm{Re}^m$, where the exponent is cited as m=0.565. In the current study, data are found to collapse

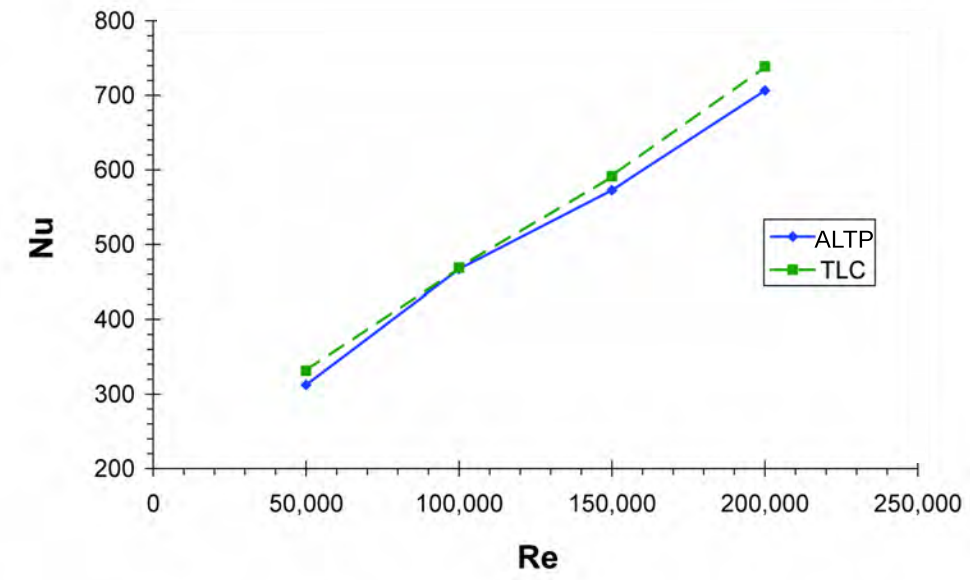

(a)

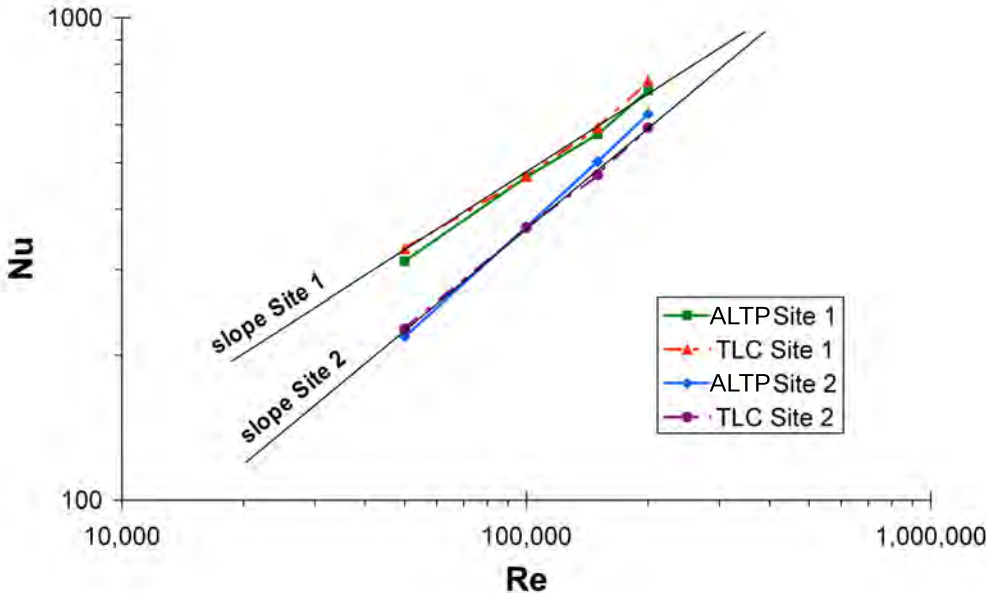

(b)

Figure 3.3: Variation in the Nusselt number with Reynolds number (a) for Site 1 of the heat-flux sensor; (b) for Sites 1 and 2 in log-log scale. [62]

resulting from a least-squares fit using

$$Nu = 0.69Re^{0.565} \tag{3.8}$$

In this case, the Reynolds number is based on the channel hydraulic diameter. This normalization flattened out the results, thus demonstrating the applicability of this relation

for the given flow conditions.
For Site 2, an exponent of about m=0.7 is found using the same normalization. This value is closer to the exponent for turbulent channel or boundary layer flow compared with Site 1. Further discussion on this subject including references can be found in [62].

Time-resolved results and spectra. Time-resolved results are analyzed from the ALTP heat-flux sensor for both Sites 1 and 2 to obtain spectra of the turbulent heat flux and to obtain turbulent heat-flux intensities and turbulence length scales. Heat flux results are corroborated by measurements of the velocity in identical experiments using a flush mounted hot-film probe at Site 1, with data taken for several Reynolds numbers. A time trace of the heat flux and velocity is shown in Figure 3.4(a), where high-frequency fluctuations and the influence of large-scale structures can be seen in both traces. Since the data are taken during separate experiments, no direct correspondence may be inferred from the time signals; however, the period of large-scale (low-frequency) fluctuations appears to be similar for the two traces. Spectra for the hot-film probe are shown in Figure 3.4(b) for channel Reynolds numbers of Re=50,000, 100,000, and 150,000 at Site 1. The increase in energy is evident with increasing Reynolds number, as is the extension of the inertial subrange to higher frequencies. With increasing Reynolds number, the slope of the power spectral density approaches the universal -5/3 law expected for isotropic turbulence in the non-viscous inertial subrange. Turbulence intensity of the velocity fluctuations is calculated at about Tu=20% for all Reynolds numbers. Autocorrelation of the time-resolved results provides integral time scales on the order of 1 ms using Equations 3.3 and 3.4. Since the flow at the measurement location is similar to a jet stagnation point flow,

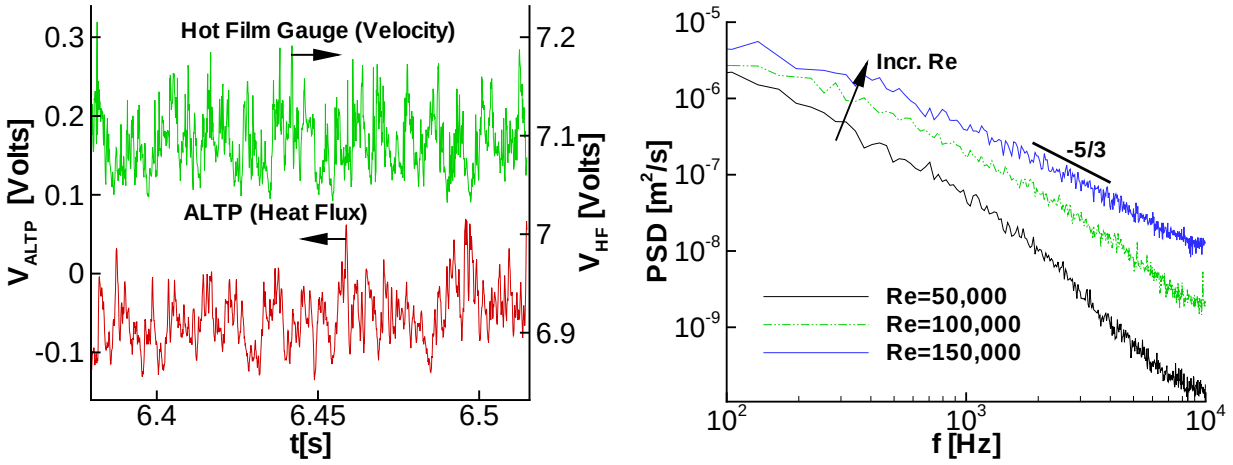

(a) (b)

Figure 3.4: (a) Heat-flux and velocity time signals at Site 1 for Re=100,000; (b) Power spectral density of velocity versus frequency using a hot-film probe at Site 1.

the assigned bulk channel velocity is used to calculate an integral length scale based on a representative velocity (Eqn. 3.5). This results in an integral length scale of about Λ_f =25 mm=0.60 W at a channel Reynolds number of Re=100,000. This indicates that the energy containing eddies are of a size a little larger than half the width of the channel. An estimate of the frequency of the Kolmogorov scale is made using Equations 3.6 and 3.7, resulting in a frequency of about 3×10^4 Hz for a channel Reynolds number of Re=100,000. This frequency is just to the right of the range of frequencies shown in Figure 3.4(b).
Frequency domain results for the heat flux shows similar trends. As seen in Figure 3.5(a), the slope of the power spectral density also decreases with increasing Reynolds number, approaching a value of about m = -2.4 at a Reynolds number of Re=200,000. Lumley [80] suggests by dimensional analysis that the heat flux should follow a universal -7/3 law. The current results approach this suggested power law at the highest Reynolds numbers, thus reinforcing the evidence that a power-law behavior is universal in the heat-flux spectra as well. The heat-flux spectra in the figure also show an increase in total energy in the flow with increasing Reynolds number and an increase in the extent of the inertial subrange. The turbulent heat-flux intensity Tu_q, which is found to be about Tu_q=20% for all Reynolds numbers. This relatively high value for the turbulent heat-flux intensity indicates that turbulence plays a large role in the augmentation on the mean heat flux at this location on the wall. Integral time scales on the order of 1 ms are calculated from the time signal, similar to the velocity signal. However, the integral length scale from the heat flux for a channel Reynolds number of Re=100,000 is calculated to be about Λ_q=15 mm, or 35% of the channel width. This indicates that the most energetic eddies related to the heat flux are somewhat smaller than those in the turbulent velocity field. Although the heat-flux sensor is influenced most strongly by fluctuations in the channel axial direction, i.e., directed at the tip wall, it appears that the large scale eddies affecting the heat flux are bound by the channel width and the region of circulation of the secondary flows.
The ratio of the velocity integral length scale to the heat-flux integral length scale, which may be interpreted as the turbulent Prandtl number (Schlichting [126])

$$Pr_{turb} = \frac{\Lambda_f}{\Lambda_q} \tag{3.9}$$

has a value at the wall of 1.67 at Site 1 for a channel Reynolds number of Re=100,000, which is in the range of values measured close to the wall for boundary layers and obtained from simple models shown by Kays et al. [65]. Behavior of the spectra at Site 2 is similar to that at Site 1, but the spectra contain less energy at all Reynolds numbers. A comparison between spectra measured at Sites 1 and 2 for a Reynolds number of Re=100,000 is shown in Figure 3.5(b). The difference in energy at lower frequencies can be clearly seen, while the spectra both trail off at the same higher frequency. The data also show that, even at

this lower Reynolds number, the spectra approach the -7/3 law. The spectra follow the same trends with Reynolds number for Site 2 as those shown in Figure 3.5(a) for Site 1, but with lower energy at each Reynolds number. As for Site 1, the integral length scale is relatively large with a value of about Λ_q=15 mm=0.35 W at a channel Reynolds number of Re=100,000. This would be expected since the flow is constrained in the same fashion approaching both positions. At Site 2, the turbulent heat-flux intensity is found to be a little higher than Tu_q=20% for all Reynolds numbers.

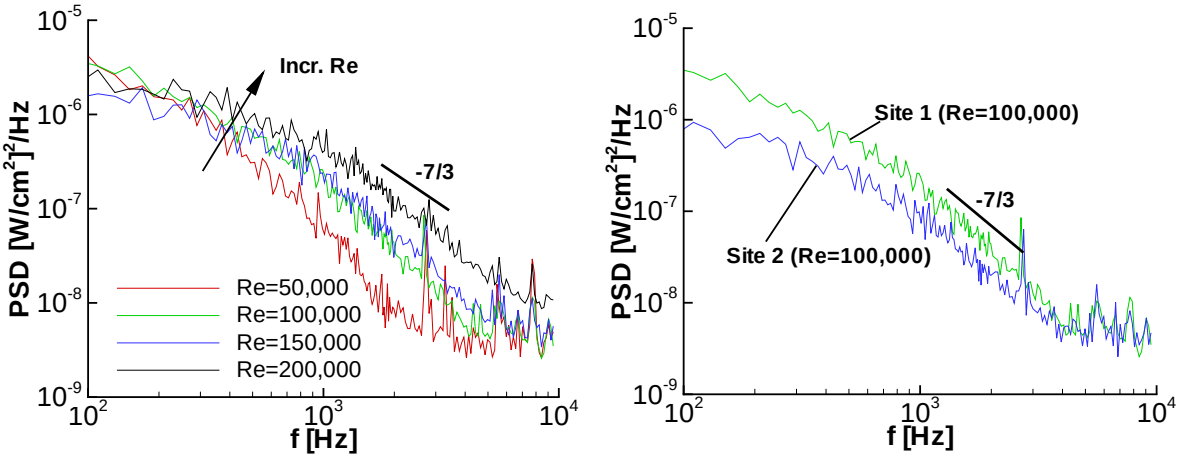

(a) (b)

Figure 3.5: Power spectral density of heat flux versus frequency using the ALTP sensor (a) at Site 1; (b) comparing Sites 1 and 2 at Re=100,000.

Conclusions. Quantitative comparisons between results from a transient liquid-crystal technique and the ALTP show very good agreement for two positions on the tip wall. Analysis of the variation in heat transfer with the Reynolds number demonstrate differences in the behavior of the flow field responsible for the heat flux at these locations. At the position of peak heat transfer on the inflow side of the tip wall (Site 1), the variation in Nusselt number with Reynolds number follows a trend more like that for jet stagnation point flow. At Site 2 on the outflow side of the tip wall, the trend is more similar to that found in turbulent channel or boundary-layer flow.

Analysis of the time signal from a flush mounted hot-film probe at Site 1 on the tip wall shows that the velocity spectrum approaches the universal -5/3 power-law behavior for higher Reynolds numbers. Similar results for the same position for the heat flux shows that the spectra has a -7/3 slope in the nonviscous inertial subrange, consistent with dimensional analysis. Turbulence intensities of the velocity and heat flux are both 20%. Length scales are determined using the time signals and an estimated bulk velocity. Results show the velocity integral length scale is 60% of the channel width, while the

heat-flux integral length scale is 35% of the channel width, resulting in a ratio of integral length scales (turbulent Prandtl number) at the wall of Λ_f /Λ_q=1.67. These results show the importance of turbulence on the tip wall heat transfer in internal ribbed channels. The combination of two-dimensional optical measurement techniques with point-wise, time-resolved heat-flux measurements lead to greater understanding of the influence of fluctuations in temperature fields and heat transfer mechanisms. This procedure can be improved by the simultaneous use of multiple ALTP sensors resulting into a direct and more precise determination of an integral length scale.

3.1.3 Remarks on the Suitability of ALTP Sensors for Turbomachinery Studies

In perspective of the current results, the ALTP sensor should be suitable for other short or long duration turbomachinery investigations, where other gauge type sensors have been used in the past (see e.g. Haldeman and Dunn [47], Iliopoulou et al. [59], Holmberg and Diller [57] and the review by Dunn [27]). Although the thermal stability of the sensor should be addressed for these applications in the case of larger temperature differences than given in the presented benchmarks, the heating of the sensor should be relatively small, at least in the first few milliseconds of a short duration run since the sensor does not require active heating of the film. Due to the fast frequency response of the sensor, this relatively short data acquisition period should normally be sufficient. However, the disadvantages of most wall-mounted surface sensors such as casing effects and conduction errors (see also sec. 2.3) due to the insertion of a low conductivity substrate in a metallic surface, as well as durability in flows that are not entirely clean would also apply for the ALTP sensor.

3.2 Heat Transfer and Pressure Measurements on the Surface of a Low-aspect-ratio Circular Cylinder

The flow over a finite-height cylinder has been the subject of extensive studies by means of various experimental techniques for many years. A summary of previous work is given by Pattenden [104] in 2005. The reader is referred to this summary for references in a wide regime of Reynolds numbers and range of aspect-ratios. The mean flow topology at the surface of a low-aspect ratio cylinder can be divided into three areas: the horseshoe vortex system in the lower part, the middle part dominated by the separating shear layer and finally the flow over the free-end strongly influenced by the development of a tip

vortex system.

Convective heat transfer studies of a finite cylinder are fairly sparse and mostly concerning the local but not time-resolved measurements of heat transfer characteristics. The correlation between heat-flux and pressure fluctuations touches the subject of the analogy between heat and momentum transport. The oldest theory concerning this analogy was stated by Reynolds, who assumed that there is a complete analogy between these quantities. Hinze describes in [55] that if such an analogy existed, it would be possible to calculate the mean velocity distribution and to obtain a relation between the coefficients of heat transfer and wall friction. Evidence is also shown in [55] for the correlation of wall pressure fluctuations with the mean wall shear stress, which closes the circle and would deliver a quantitative framework for the comparison of heat-flux and pressure fluctuations under certain conditions. A quantitative level of comparison of heat and pressure fluctuation is not the subject of this study, only qualitative correlation of these quantities will be presented (see also Roediger et al. [119]).

3.2.1 Experimental Setup

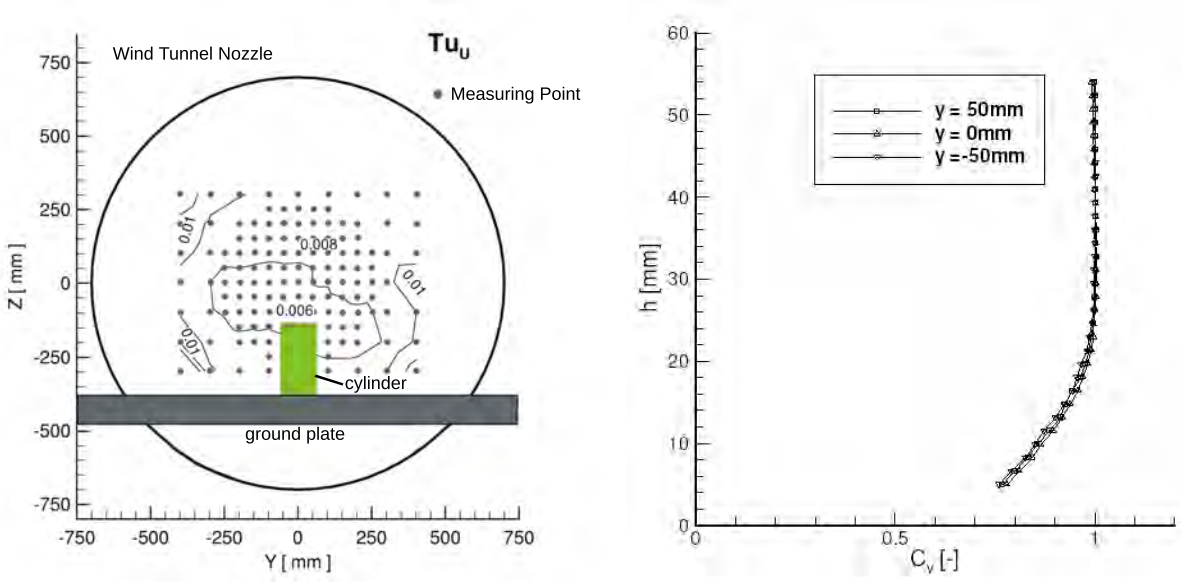

(a) (b)

Figure 3.6: (a) Turbulence Intensity (view in flow direction); (b) Velocity profiles in the y-plane of cylinder. [6]

Wind tunnel and cylinder model. The experiments are performed in a closed circuit wind tunnel with an open test section. The installed nozzle with an exit diameter of 1.4 m

allowed maximum free-stream velocities of about 37 m/s. The turbulence level in the test section flow is approximately 0.8 % (see Fig. 3.6(a)).
The cylinder model has an aspect ratio of H:D=2:1 with a height H=240 mm and diameter D=120 mm. The x, y and z axes are in the streamwise, transverse and spanwise directions, respectively. The model is mounted on a ground plate, which had an elliptic leading edge 1220 mm upstream of the z-axis of the cylinder.
The boundary layer (BL) on the ground plate develops naturally and the measured velocity profile indicates a BL thickness of $\delta/H = 0.092$ at the model position (see Fig. 3.6(b)).

Surface pressure measurements. The disassembled model used for the pressure measurements is shown in Figure 3.7 (a). It has 79 pressure tappings along a generator of the cylinder with a distance of 3 mm. Another 39 pressure tappings are located along a center line on the top surface of the model with the same spatial resolution of 3 mm. The model

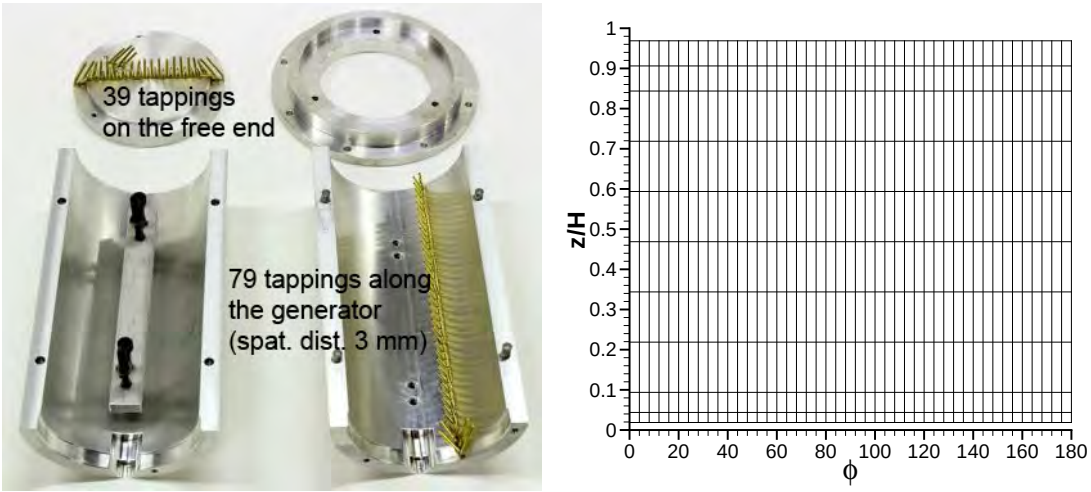

(a) (b)

Figure 3.7: (a) Disassembled cylinder model with pressure tappings; (b) measuring grid for pressure fluctuation measurements (only every fifth line plotted on ϕ-axis).

could be rotated by a servo driven table with a minimal increment of 0.2°.
For the static pressure measurements a Scanivalve-Module (DSA 3217) with 16 channels and a pressure range of 2500 Pa at a maximum scanning rate of 200 Hz is used. Elastic hoses of 1 m length connect the module to the pressure tappings. The model is rotated on the base through 360° at 5° intervals and refined at angles between 50 - 90° and 270 - 310° to an increment of 2°.
Simultaneous pressure fluctuations are measured by a set of 12 single pressure transducers mounted inside the cylinder. The sensors used are piezoresistive gauges (Keller PD-4E)

with a pressure range of 3000 Pa. The gauges are installed with a tube length of 60 mm between the gauge and the cylinder surface. This represents the minimal possible distance in order to achieve a minimum in damping of the pressure fluctuations. The gauges are not evenly distributed along the generator of the cylinder but concentrated at the top and the bottom to obtain a finer spatial resolution at the free-end and in the region influenced by the ground plate. The distribution of the gauges is shown in the measuring grid in Figure 3.7 (b). The cylinder is rotated on the base through 360° at 1° intervals. On the free-end the pressure transducers are evenly distributed along the radius of the cylinder.

Heat-flux measurements. In the present experiments, an ALTP sensor with a protective coating and an active area of $3 \times 3\,\mathrm{mm}^2$ is used. The sensor module (see sec. 2.4) with a flat surface forms a maximal roughness of 0.13 mm on the surface of the cylinder. The ALTP measurement positions are evenly distributed along the generator of the cylinder at z/H = 0.18; 0.38; 0.58; 0.78. On the free-end the ALTP gauges are located at r/R=0.24; 0.34; 0.5; 0.58; 0.66; 0.8 along the radius of the cylinder, where R=D/2.
In order to achieve a temperature gradient in the incompressible BL of the cylinder, the model is heated by an external heating system mounted below the cylinder model under the tunnel floor. A variable air flow rate between 4 - 10 m^3/h is forced past a heating cartridge with a nominal maximum power of 1500 W. The air heats the wall of the cylinder to an excess temperature difference of approximately $\Delta T \approx 20$ - 25 K at $\mathrm{Re}_D = 2 \times 10^5$. The temperature distribution measured by an infrared camera shows a wall temperature difference of ~ 5 K between the free-end and the lower part of the cylinder. The cylinder and the heating system are insulated from the wooden base to minimize the heating of the wake and inflow BL. It is rotated on the base through 360° at 5° intervals after the equilibrium temperature of the cylinder was established.
The effect of the convection on the topology compared to the unheated case is studied by comparative temperature fluctuation measurements with a wall-mounted hot film gauge used as temperature resistance thermometer (Dantec Flush Mounting Probe 55R45 operated in constant current mode). The local shift of the fluctuation peak is minimal and within the measuring accuracy of this technique. Thus, the influence of the convection on the BL on the surface is minimal. Possible effects on the wake when the cylinder is heated, however can not be excluded.

Surface flow visualization. Oil-flow visualization is carried out in order to study the basic topology of the flow around the circular cylinder wall at $Re_D = 2 \times 10^5$. A mixture of neon green colored particles and oleic acid is used. The tunnel is run for several minutes until a steady flow pattern is established. The pattern is then photographed with a

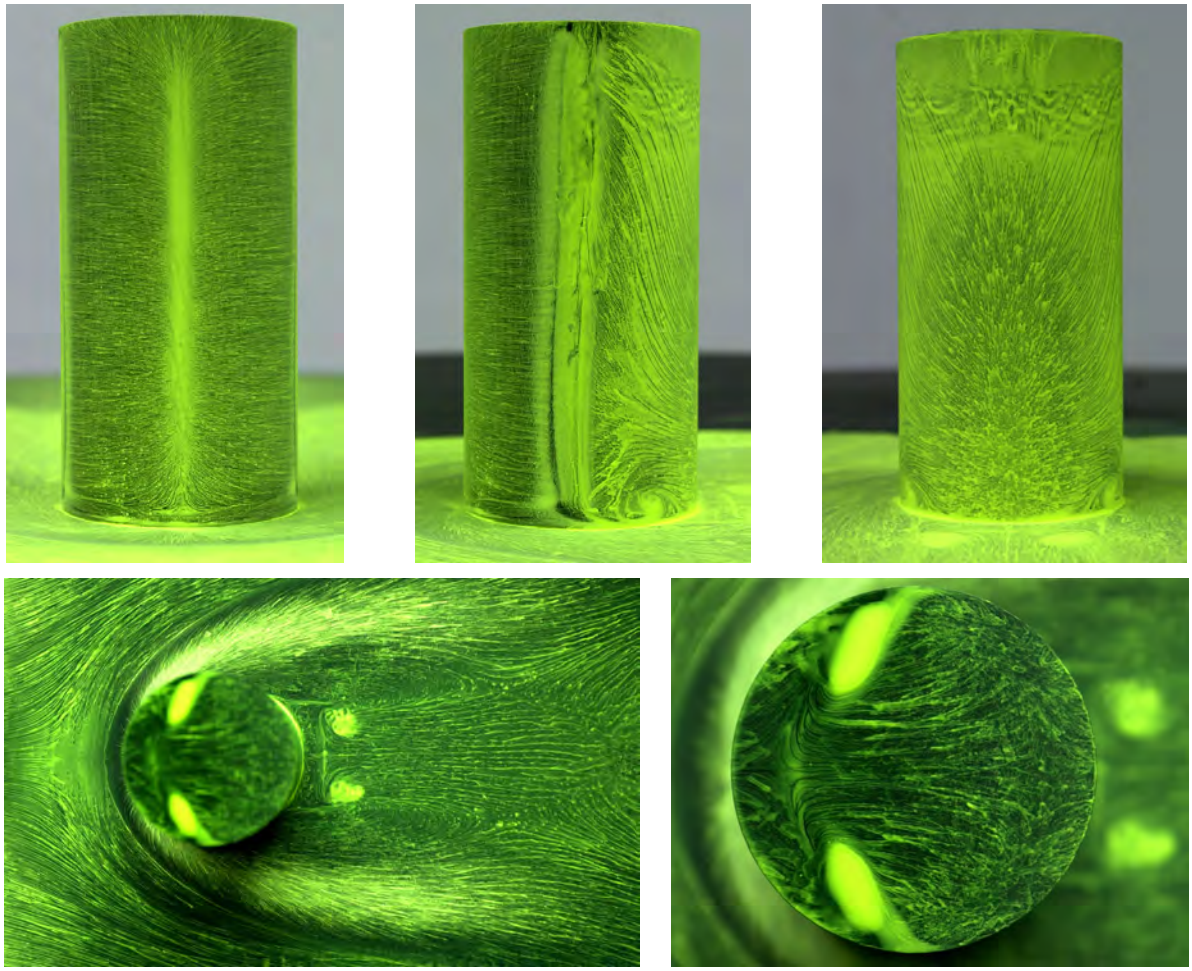

Figure 3.8: Oil-film visualization images for $\mathrm{Re}_D = 2 \times 10^5$. Top row (from left to right): Front view, Side view (flow from left to right), Rear view. Bottom Row: Top views (flow from left to right): Floor of tunnel, Free-end of cylinder.

standard high resolution digital camera with the model in situ. The images (Fig. 3.8) give an insight in the present flow phenomena around the cylinder and at its free-end. In the front and side view the stagnation line and the line of separation respectively are clearly visible. The foot-print of the horse-shoe vortex on the ground can be clearly identified. The rear view displays the three dimensional signature of the wake region induced by the free-end flow. The top view shows the extent of the wake and several dominant vortical structures. The detailed view of the free-end illustrates the bases of two vortices on the surface as dominant foci and a crescent-shaped region in the rear half of the free end.

3.2.2 Experimental Results

Static pressure distributions. To study and identify the flow topology of the cylinder flow in a wider Reynolds number range, static pressure measurements are carried out

for the Reynolds numbers $\mathrm{Re}_D = 1 \times 10^5$, 2×10^5 and 2.3×10^5. Fig. 3.9(a-c) show the normalized static pressure distributions around the cylinder, where $c_{ps} = 2(\mathrm{p\text{-}p}_\infty)/(\rho\,\mathrm{u}_\infty)$ represents the static pressure coefficient and ϕ is the angular position of the pressure tapping row in reference to the stagnation line.

Some typical features of the low aspect-ratio cylinder flow topology are visible in the distributions. At $\phi = 0°$ the pressure coefficient near the top is reduced due to the upwash over the tip. The influence of the horseshoe vortex in the lower region z=0 - 0.1 H of the cylinder is clearly visible by a kink in the pressure coefficient. In comparison to an infinite cylinder, the separation occurs further upstream on the surface. For example, at $\mathrm{Re}_D = 2 \times 10^5$ an angle of 80° is expected for the infinite cylinder, the pressure measurement on the low-aspect ratio cylinder, however, yields an angle of about 65 - 70°. This feature was also observed by Pattenden et al. [104] and is attributed to the higher pressure behind the cylinder created by the free-end flow entering into the recirculation region. At separation, the magnitude of the minimal pressure coefficient decreases with increasing Reynolds number from $c_{ps} \approx -0.8$ at $\mathrm{Re}_D = 1 \times 10^5$ to $c_{ps} \approx -2$ at $\mathrm{Re}_D = 2.3 \times 10^5$. In addition, the separation line shifts further downstream and the region of minimal pressure moves towards the middle of the cylinder with increasing Reynolds number. For $\mathrm{Re}_D < 2 \times 10^5$, the region of minimal pressure broadens towards the tip of the cylinder and the flow separation is delayed for several degrees. At the back of the cylinder, the pressure coefficient clearly rises towards the base. This is caused by the reverse flow of the wake impinging on the surface. For $\mathrm{Re}_D = 2.3 \times 10^5$, the BL at the surface has undergone transition and the turbulent BL can sustain higher pressure gradients, hence the separation line moves further downstream.

In the following the investigations will be concentrated on the critical Reynolds number $\mathrm{Re}_D = 2 \times 10^5$. Its flow topology will be studied in more detail by the comparison of pressure and heat-flux fluctuations.

Distributions of pressure and heat-flux fluctuations. Fluctuation distributions are of special interest for the detection of BL transition on a surface. Close to the critical Reynolds number, the BL over the surface of the cylinder is laminar and transition is occurring in the shear layer immediately after the separation. Thus, strong fluctuation should appear in this region.

Figure 3.9(d) displays the distribution of pressure fluctuations $c'_{ps} = 2(\mathrm{p'\text{-}p}_\infty)/(\rho\,\mathrm{u}_\infty)$ around the cylinder. The maximum fluctuations occur at about 95°. Towards the free-end the maximum is shifted downstream which correlates with the delayed separation observed in the static pressure distributions. In the back of the cylinder the magnitude of fluctuations increases towards the base. The distribution in Figure 3.10(a) shows the

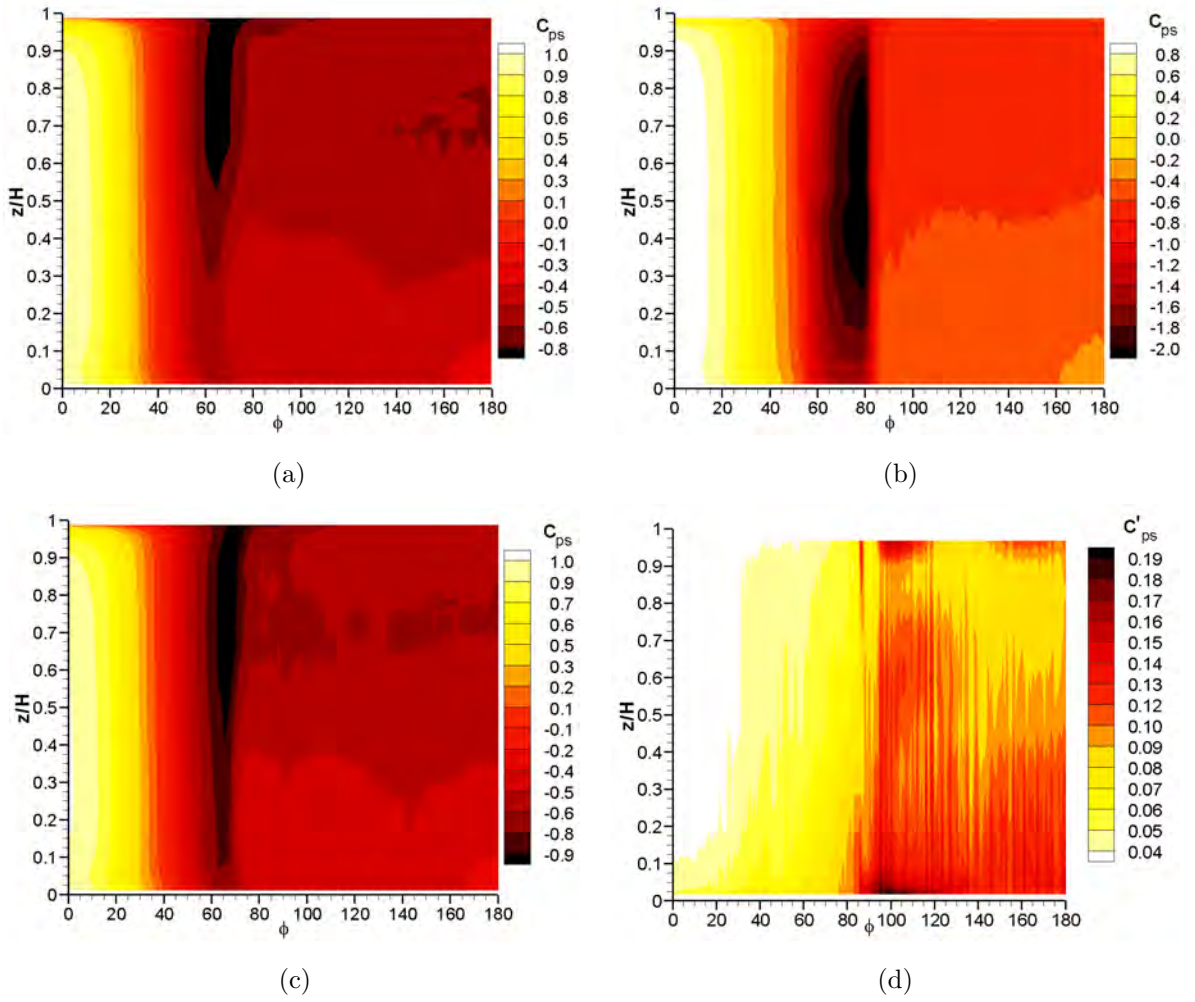

Figure 3.9: Distribution of pressure coefficient c_{ps} around the cylinder at (a) $\mathrm{Re}_D = 1 \times 10^5$, (b) $\mathrm{Re}_D = 2.3 \times 10^5$ and (c) $\mathrm{Re}_D = 2 \times 10^5$; (d) distribution of pressure fluctuations c'_{ps} at $\mathrm{Re}_D = 2 \times 10^5$.

maximum heat-flux fluctuations at the same angle of about 95°. The maximum is however more pronounced in relation to the pressure fluctuations. This might be caused by the damping of the flexible pressure hoses. Time-resolved wall pressure measurements by surface-mounted micro electromechanical pressure sensors confirm the existence of this more pronounced pressure peak on a cylinder of the same geometry (Wolter et al. [150]). Figure 3.10(b) displays power spectra around the cylinder at a horizontal plane of $z/H = 0.91$. Frequencies up to 1 kHz are plotted; no significant heat-flux fluctuations could be detected beyond this frequency. The spectral distribution shows a peak at about 95° caused by an increase of the intensity level in a frequency range up to 800 Hz. Beyond that point the range of dominant frequencies decreases again but stays above the level of the laminar BL before transition. This spectral distribution is qualitatively very similar to a typical pressure fluctuation spectrum.

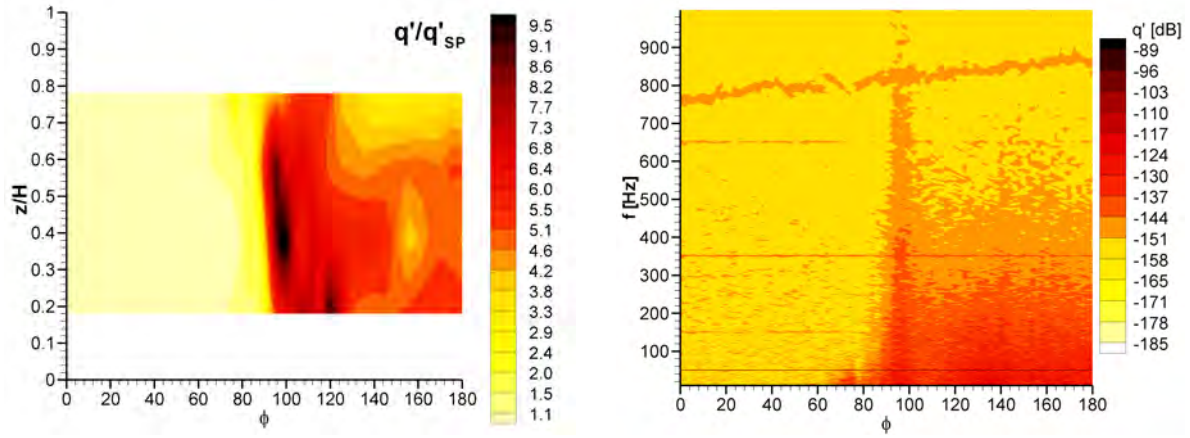

(a) (b)

Figure 3.10: Distribution of (a) normalized heat-flux fluctuations q'/q'_{SP} and (b) power spectra at plane $z/H = 0.78$ around the cylinder at $\mathrm{Re}_D = 2 \times 10^5$.

In general, a qualitative correlation of the pressure and heat-flux fluctuation around the cylinder is visible and the detection of transition by means of heat-flux and pressure fluctuation is successfully demonstrated.

Free-end flow. The flow over the free-end is dominated by separation from the sharp leading edge. The oil-film visualization in Figure 3.8 shows the complex 3D recirculation region on the top of the cylinder. Two foci dominate the front part and mark the origin of two counter-rotating vortices. The rear part of the free-end shows a crescent-shaped

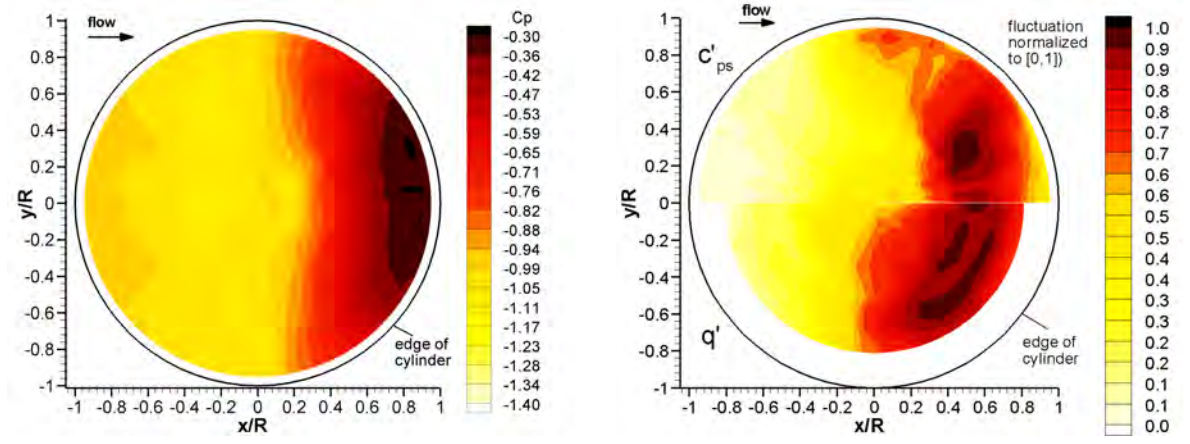

(a) (b)

Figure 3.11: (a) Distribution of pressure coefficient c_{ps} and (b) comparison of normalized pressure and heat-flux fluctuations on the free-end surface at $Re_D = 2 \times 10^5$.

footprint. The topology of this zone has been discussed controversially in Pattenden et al. [104] and Roh & Park [123]. The oil-film visualization seems to confirm the flow pattern proposed by Roh & Park [123], who suggest the existence of a separation saddle point between two attachment nodal points in this region.
The static pressure distribution in Figure 3.11(a) displays an extensive low pressure region in the front part of the free-end. The pressure minimum is located in the center of the two foci transporting fluid away from the surface. Towards the rear part the surface pressure rises significantly and an area of higher pressure is formed in its second half. The static pressure distribution does not capture the character of this highly unsteady region very well. The fluctuation measurements in Figure 3.11(b) illustrate much better the crescent-shaped footprint observed in the oil-film images. This figure compares the normalized pressure fluctuations (upper half) with the heat-flux fluctuations measured by ALTP gauges (lower half). Both types of fluctuations A' are normalized to an interval [0, 1] for better comparison, i.e. the fluctuations were transformed to a ratio of differences according to the relation $(A' - A'_{min})/(A'_{max} - A'_{min})$. The images show maximum fluctuations along a radius of about $r/R = 0.6$ in the rear part of the free-end. The region of high pressure fluctuations is smaller than the one covered by the ALTP measurements. The measured heat flux fluctuations extend further upstream and reach from the center towards the edges of the free-end. The pressure fluctuations, however, are more concentrated towards the center line. The features are probably caused by the higher temporal resolution of the ALTP in comparison to the pressure transducers. The observation might indicate that the dominant frequencies at the edge of this unsteady region are shifted towards higher values.

Conclusions. The flow topology of a finite-length circular cylinder with the aspect ratio 2 is used to study the qualitative correlation between heat-flux and pressure fluctuation. Static pressure measurements in a Reynolds number range between $\mathrm{Re}_D = 1 \times 10^5 - 2.3 \times 10^5$ allow an identification of the major flow phenomena in combination with oil-film visualization at $\mathrm{Re}_D = 2 \times 10^5$. These measurements help to identify dominant features in the fluctuation distributions of heat flux and pressure. A correlation of the maximum pressure and heat-flux fluctuations is found at the transition of the separated shear layer around the cylinder. The spectra of the heat-flux fluctuation show an increase of the intensity level in a frequency range up to 800 Hz at transition location. The pressure and heat-flux fluctuation peaks in the rear part of the free-end are in good agreement and show the importance of time-resolved measurements for the study of unsteady flow phenomena.